



Boosting visible light photocatalysis in an Au@TiO₂ yolk-in-shell nanohybrid

Jun Hu^a, Rufang Zhao^a, Haitao Li^{a,*}, Zhilong Xu^a, Han Dai^b, Hua Gao^c, Hongjian Yu^d, Ziyao Wang^a, Yang Wang^a, Yan Liu^a, Jie Han^{a,*}, Rong Guo^a

^a School of Chemistry and Chemical Engineering, Yangzhou University, Yangzhou 225002, China

^b Yantai Nanshan University, Longkou, Shandong Province 265713, China

^c School of Science, China University of Geosciences, Beijing 100083, China

^d Beijing Key Laboratory of Materials Utilization of Nonmetallic Minerals and Solid Wastes National Laboratory of Mineral Materials School of Materials Science and Technology China University of Geosciences, Beijing 100083, China

ARTICLE INFO

Keywords:

Yolk-shell
Yolk-in-shell
Nanocatalyst
Visible light photocatalysis
Hydrogen production

ABSTRACT

Yolk-shell nanohybrids have garnered increasing interests in many applications, such as in catalysis, energy, and molecular sensing. However, their intrinsic architectural limitations have led to insufficient synergistic effects and instability which are unfavorable for nanocatalysis. Designing a unique yolk-in-shell nanostructure where the “yolk” is embedded in the “shell” can overcome this challenge to boost nanocatalysis. Herein, an unprecedented Au@TiO₂ yolk-in-shell nanocatalyst has been developed to dramatically improve the visible light photocatalysis. The as-designed Au@TiO₂ nanohybrid displays an efficient hydrogen-production (95.6 mmol h⁻¹ g⁻¹, Au: 0.04 wt%), 3- and 14-times better than conventional Au@TiO₂ yolk-shell nanostructure and pure TiO₂ hollow nanosphere, respectively. Our unique design also notably achieves high selectivity (~100%) towards CO production (0.75 mmol h⁻¹ g⁻¹) under visible light irradiation. This unique yolk-in-shell nanoarchitecture promises enormous opportunities for the design of next-generation hybrid nanocatalysts with enhanced catalytic performances.

1. Introduction

Yolk-shell nanostructures have demonstrated unique advantages over other elaborate designs, especially the corresponding core-shell configuration [1–13]. Notably, yolk-shell nanostructures with noble metal nanoparticles as the yolk have attracted tremendous interest [14–18] because its position within the interior environment can be tuned to (1) optimize the balance between efficiency and stability [19, 20], (2) improve mass transfer to the encapsulated catalyst [21,22], and (3) easily modulate synergistic effect [23]. Despite their advantages, yolk-shell designs suffer from limited contact efficiency between yolk and shell [24], undesired barrier effect from shell, and adverse aggregation of yolks due to structural damage [25,26]. These limitations severely hinder their application in catalysis.

To overcome these challenges, various strategies involving the engineering of the shell, yolk, and void have been developed [27–33]. Among them, the embedding of the active yolk center existing in the shell to achieve yolk-in-shell hybrids is fast emerging as an attractive

approach to overcome the inherent issues in conventional yolk-shell configuration while retaining the original advantages. This unique yolk-in-shell design allows full contact between the yolk and shell, thereby enabling additional synergistic effects from the interfacial chemical interactions and avoid aggregation of active centers in case of broken shell [27,28]. Additionally, the barrier effect on the active center can be weakened by tuning the shell thickness. Such structural advantage for yolk-in-shell nanohybrids has been demonstrated in our previous proof-of-concept study by classical model reaction [28]. However, this well-established design is still lack of comprehensive display of structural advantages and extensive applications. Thereby, a rational yolk-in-shell nanocatalyst should be further investigated to further exemplify its unique advantages and bridge the gap between theory and practice.

Herein, a class of yolk-in-shell nanohybrid based on a single Au nanoparticle and TiO₂ nanocavity (Au@TiO₂), fabricated via electrostatic adsorption and template method, has been first demonstrated as outstanding nanocatalyst for visible light photocatalysis. The Au@TiO₂

* Corresponding authors.

E-mail addresses: htli@yzu.edu.cn (H. Li), hanjie@yzu.edu.cn (J. Han).

<https://doi.org/10.1016/j.apcatb.2021.120869>

Received 8 August 2021; Received in revised form 2 October 2021; Accepted 27 October 2021

Available online 1 November 2021

0926-3373/© 2021 Elsevier B.V. All rights reserved.

yolk-in-shell nanohybrids with adjustable shell thickness (10–50 nm) were selected as visible light photocatalyst to study and demonstrate their catalytic performance. A shell thickness has been optimized at 30 nm for the unique Au@TiO₂ yolk-in-shell nanostructure. Compared with the related Au@TiO₂ yolk-shell nanohybrids and pure TiO₂ nanocavity, the unique Au@TiO₂ yolk-in-shell nanohybrids have drastically boost H₂- and CO-production under visible light irradiation. The enhanced catalytic performance in Au@TiO₂ yolk-in-shell nanohybrids arises from the intimate integration of the yolk and shell structures, more easily excited surface plasmon resonance (SPR) as further confirmed using finite difference time domain (FDTD) simulations, as well as effective hot electron transfer verified by the first-principles calculations. The yolk-in-shell configuration thus clearly yields high-performance nanocatalysts that are highly demanded in many practical applications. This nanoarchitectural design will provide a critical reference for the structural optimization of catalytic nanomaterials for advanced nanocatalysis.

2. Experimental

2.1. Chemicals

Chloroauric acid (HAuCl₄·3H₂O, 98%), tetraethyl orthosilicate (TEOS, 98%), Tetrabutyl orthotitanate (TBOT, ≥ 97.0%), triethanolamine (AR), polyvinylpyrrolidone (PVP-10, average molecular weight (MW)= 10,000), and (3-aminopropyl) triethoxysilane (APTES, 99%) were purchased from Sigma-Aldrich. NaOH (≥ 97.0%, pellets), ammonia (14% w/w), acetonitrile (≥ 99.9%) and anhydrous sodium sulfate (99.9%) and other chemicals (analytical pure) were purchased from Sinopharm Reagent (Shanghai, China).

2.2. Synthesis of Au@SiO₂ core-shell nanocomposites

Chloroauric acid aqueous solution (305 μL, 0.1 mol L⁻¹) and trisodium citrate aqueous solution (6 mL, 0.005 mol L⁻¹) were added in 30 mL boiling water, successively, then reflowed for half an hour. After cooling to room temperature, PVP-10 (0.235 mL, 12.8 g L⁻¹) was added, and the obtained colloidal solution was stirred for 12 h. This colloid solution was then centrifuged and redispersed in 4 mL aqueous solution for further use. Subsequently, 0.55 mL Au solution was mixed with 3 mL H₂O, 0.5 mL ammonia, and 20 mL isopropanol, and keeping stirring for half an hour. Afterwards, 0.0625 μL TEOS was added to the reaction system every hour within 4 h. Ultimately, the Au@SiO₂ core-shell nanoparticles were obtained through washing with deionized water 3 times and then were dried at 60 °C for 12 h.

2.3. Synthesis of SiO₂-NH₂ nanoparticles

24 mL TEOS was slowly added into the mixed solution containing 480 mL ethanol, 40 mL H₂O, and 12.8 mL ammonia, followed by vigorous stirring at room temperature for 24 h to receive SiO₂ nanoparticles. The achieved SiO₂ nanoparticles were purified by washing 3 times with deionized water and ethanol, and then were dried at 60 °C for 12 h. To further prepare SiO₂-NH₂, 1.0 g SiO₂ nanoparticles were dispersed with boiling isopropanol (150 °C), followed by addition of 0.4 mL APTES, and the solution was then reflowed for 12 h. Finally, the products were purified by washing 3 times with deionized water and ethanol, then dried at 60 °C for 12 h.

2.4. Synthesis of Au@SiO₂ Janus nanoparticles

75 mg SiO₂-NH₂ nanoparticles were first dispersed in aqueous solution (30 mL), followed by adding Au colloidal solution (0.55 mL). Then, the mixed solution was stirred at room temperature for 2 h. Finally, Au@SiO₂ Janus nanoparticles were received by washing with deionized water 3 times and drying at 60 °C for 12 h.

2.5. Synthesis of Au@TiO₂ yolk-in-shell nanostructures

80 mg Au@SiO₂ Janus nanoparticles were dispersed with 25 mL ethanol, 7 mL acetonitrile and 0.2 mL ammonia in a beaker, and the solution was stirred for 0.5 h. 0.5 mL TBOT was then added slowly into precursor solvent consisted of 3 mL ethanol and 1 mL acetonitrile. Afterwards, the solvent was added into the beaker and stirred for 4 h. The target products were gained by centrifugation and washed 3 times by ethanol. The obtained SiO₂@Au@TiO₂ hybrids were calcined at 500 °C (5 °C/min) for 2 h. In order to remove SiO₂ in SiO₂@Au@TiO₂ hybrids, SiO₂@Au@TiO₂ hybrids were dispersed in 20 mL NaOH (0.1 mol L⁻¹) and the solution temperature was raised to 80 °C and then stirred for 2 h. Finally, the obtained Au@TiO₂ yolk-shell nanostructures were washed 3 times with ethanol and dried at 60 °C for 12 h as visible light photocatalysts. The regulation of TiO₂ shell thicknesses (10–50 nm) in Au@TiO₂ yolk-shell nanostructures can be realized by controlling the amount of TBOT (0.2–1 mL).

2.6. Synthesis of Au@TiO₂ yolk-shell nanostructures

The synthetic procedures of Au@TiO₂ yolk-shell nanostructures were identical to those of Au@TiO₂ yolk-in-shell nanostructures, expect for the usage of Au@SiO₂ core-shell nanoparticles instead of Au@SiO₂ Janus nanoparticles. The adjustment for TiO₂ shell thicknesses (10–50 nm) in Au@TiO₂ yolk-shell nanohybrids can be achieved by controlling the amount of TBOT (0.2–1 mL).

2.7. Evaluation of visible light photocatalytic performance

2.7.1. Photocatalytic H₂-production

10 mg photocatalysts, 40 mL H₂O and 11.3 mg triethanolamine, were dispersed into the photocatalytic reactor. The hydrogen evolution was captured by gas chromatography under N₂ protection and the temperature of testing process was controlled by a thermal conductive detector (TCD). The system was measured and stirred under visible light (≥ 420 nm, CEALIGHT, GC-7920) realized by a xenon lamp (300 W, Perfectlight, China) as light source with an optical filter (λ ≥ 420 nm, UV-cut filter).

2.7.2. Photocatalytic CO₂-production

The activity of photocatalytic CO₂ reduction was detected by using a Lab solar-IIIAG closed circulation system (PLS-SXE300, Perfectlight, China) under a xenon lamp with an cutoff filter (AM1.5 G), and the reaction temperature was kept at 293 K controlled by Circulation cooling system (DC-0506, Sunny Hengping Scientific Instrument, China). Concretely, 20 mg catalyst was first dispersed evenly on the glass pane and placed on a triangle glass support in the photocatalytic reactor. 1.7 g NaHCO₃ was then put at the bottom of reactor cell followed by vacuum treatment. Subsequently, 15 mL H₂SO₄ (1.33 mol L⁻¹) was injected into the cell and reacted with NaHCO₃ powder to generate CO₂ (1 atm). Finally, 1 mL reactant gas was taken and then measured using a GC9790II gas chromatograph (Zhejiang Fuli Analytical Instrument, China) qualitatively equipped with a thermal conductivity detector (TCD) and a quadrupole-type mass spectrometer (OmniStar300).

2.8. FDTD simulations

FDTD simulations were calculated by employing FDTD Solutions 8.6.0 (Lumerical Solutions). An electromagnetic pulse ranging on 420–800 nm for the incident light was launched into a box containing the targeted Au@TiO₂ yolk-shell or yolk-in-shell nanostructures to simulate visible light interacting with the nanostructures. The overlap region of the targeted nanostructures was divided into 5 nm meshes. The related model size of yolk-shell and yolk-in-shell, were established according to TEM images as in Fig. 2a and d (diameter of Au core, inner diameter and outer diameter of TiO₂ nanospheres are 15, 200, and 260

nm, respectively).

2.9. First-principles calculations

Density functional theory (DFT) calculations were conducted by utilizing the Vienna Ab initio Simulation Package (VASP, version 5.4.4) [34,35]. The projector-augmented-wave pseudopotentials (PAW) [36, 37] were employed to describe the valence–core interaction and a kinetic-energy cutoff of 450 eV for the plane-wave basis set was adopted. The generalized gradient approximation exchange–correlation functional with Perdew–Burke–Ernzerhof (PBE) [38] was utilized for all calculations, expect that the Heyd–Scuseria–Ernzerhof functional (HSE06) [39] was chosen for calculation of band gaps. The anatase TiO₂ (101) surface was modeled as a periodic slab with three layers of oxide, and the vacuum between slabs is ~15 Å. A Monkhorst–Pack [40] 3 × 4 × 1 *k*-point grid was applied to sample the Brillouin zone. During structural optimization, all the atoms of the slab and Au atom were allowed to relax, except that two bottom layers. All geometries were fully optimized without any constraint until all atomic forces became smaller than 0.03 eV/Å.

2.10. Instruments and characterization

The morphologies and structures of the synthesized products were confirmed by field emission scanning electron microscopy (SEM, GeminiSEM 300, Britain), transmission electron microscopy (TEM, Philips Tecnai-12, Holland) and high resolution transmission electron microscopy (HRTEM, Tecnai G2 F30 S-Twin TEM, America). X-ray diffraction patterns were conducted on an X-ray diffractometer (XRD Bruker AXS D8 Advance, Germany). The specific surface area and pore size were evaluated by BET analysis instrument (BET, Beishide 3H-2000PS2, China). The composition was investigated by X-ray photoelectron spectroscopy (XPS, Thermo ESCALAB 250 spectrometer, America) and photoluminescence emission (PL, Edinburgh FLS-980, Britain) spectra. The light absorption spectroscopy was recorded using a UV-Vis-NIR spectrophotometer (DRS, Varian Carry 5000, America). Photocurrent, Mott-Schottky curves (250, 500, and 1000 Hz), and electrochemical impedance spectra (EIS) were detected by an electrochemical workstation (VMP3, Biologic, France) with three-electrode system (electrolyte solution 0.1 M Na₂SO₄). The photothermal detection for the synthesized Au@TiO₂ yolk-shell and yolk-in-shell nanocomposite were measured under simulated sunlight and recorded using an IR camera (FLIR Systems, Inc. USA).

3. Results and discussion

3.1. Synthesis and characterization

The synthetic processes of Au@TiO₂ yolk-shell and Au@TiO₂ yolk-in-shell nanohybrids are depicted in Fig. 1. The preparation of Au@TiO₂ yolk-shell nanocomposites, containing a single Au nanoparticle residing in the cavity of shell, includes three key processes (Fig. 1a): (1) a SiO₂ template (200 nm) is first coated over pre-formed Au nanoparticle (15 nm), obtaining Au@SiO₂ core-shell nanoparticle (Figs. S1a), (2) a TiO₂ shell is then coated over the Au@SiO₂ to form Au@SiO₂@TiO₂ core-shell hybrids, (3) the SiO₂ template is then removed to achieve the Au@TiO₂ yolk-shell hybrids (Fig. S1b). For the Au@TiO₂ yolk-in-shell nanostructure where the single Au nanoparticle is embedded into a mesoporous TiO₂ shell (Fig. 1b), the key is to fabricate Au@SiO₂ Janus nanoparticles which possess only one nano Au supported on the surface of each SiO₂ nanosphere (Fig. S1c). TiO₂ shell is subsequently coated on the surface of Au@SiO₂ Janus nanoparticle, leading to the formation of SiO₂@Au@TiO₂ core-shell hybrids whereby Au nanoparticle is evidently embedded in TiO₂ shell. Finally, Au@TiO₂ yolk-in-shell nanostructures can be received after removing the SiO₂ template (Fig. S1d). In addition, it is noteworthy that the shell size can be accurately regulated in the range of 10–50 nm by controlling the amount of TBOT. The advantages of Au@TiO₂ yolk-in-shell nanohybrids have been demonstrated in the application of photocatalysis, owing to its special architectural advantage.

TEM was employed to image the interior structure of designed Au@TiO₂ yolk-shell and yolk-in-shell configurations, as shown in Fig. 2. The TEM image (Fig. 2a) indicates that a single Au (diameter ~15 nm) is embedded in the cavity of TiO₂ nanosphere with 200 nm (inside) and 260 nm (outside). Moreover, HRTEM image (Fig. 2b) reveals that Au and TiO₂ possess the typical (111) and (101) crystal planes, corresponding to a crystal lattice of 0.24 and 0.35 nm respectively [17]. Moreover, the constituent Au, Ti, and O elements are clearly present in the yolk-shell nanostructure (Fig. 2c), affirming the successful formation of Au@TiO₂ yolk-shell nanohybrids. Moreover, the desired Au@TiO₂ yolk-in-shell nanostructure is shown in Fig. 2d. Similar to Au@TiO₂ yolk-shell nanohybrids, Au nanoparticle and TiO₂ nanocavity, with similar geometric structure, exhibit the characteristic (111) and (101) crystal planes respectively (Fig. 2e), suggesting that the compositions of yolk-in-shell and yolk-shell are identical. The as-prepared nanostructure was also confirmed by high-angle annular dark field-STEM image (HAADF-STEM) images in Fig. 2f. The Au@TiO₂ yolk-in-shell nanostructure is distinct whereby the single Au nanoparticle is embedded in the TiO₂ shell instead of the cavity in the yolk-shell configuration. These results therefore confirm the formation of Au@TiO₂ yolk-shell and

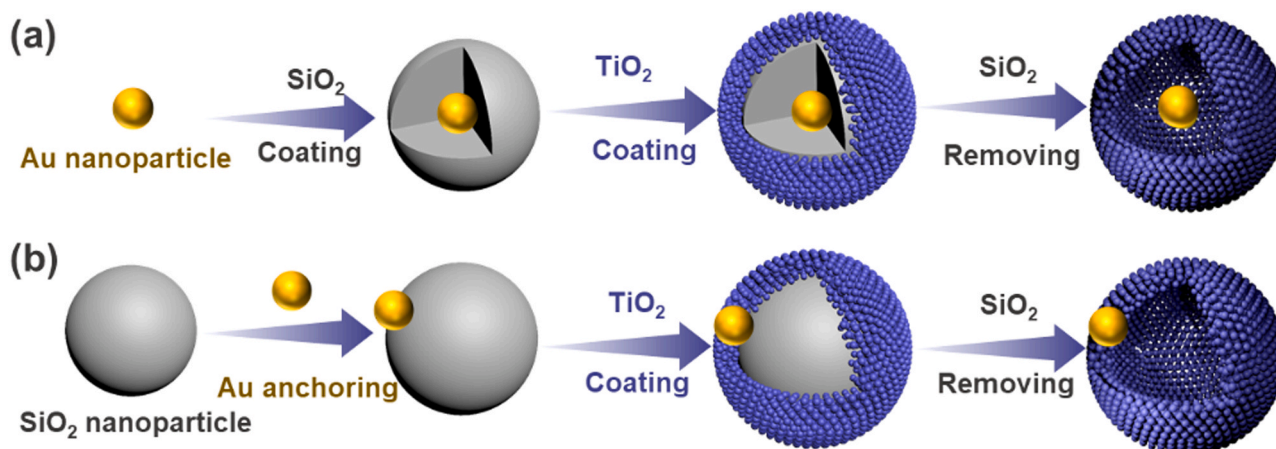


Fig. 1. Schematic illustration on the fabrication of Au@TiO₂ (a) yolk-shell and (b) yolk-in-shell nanohybrids.

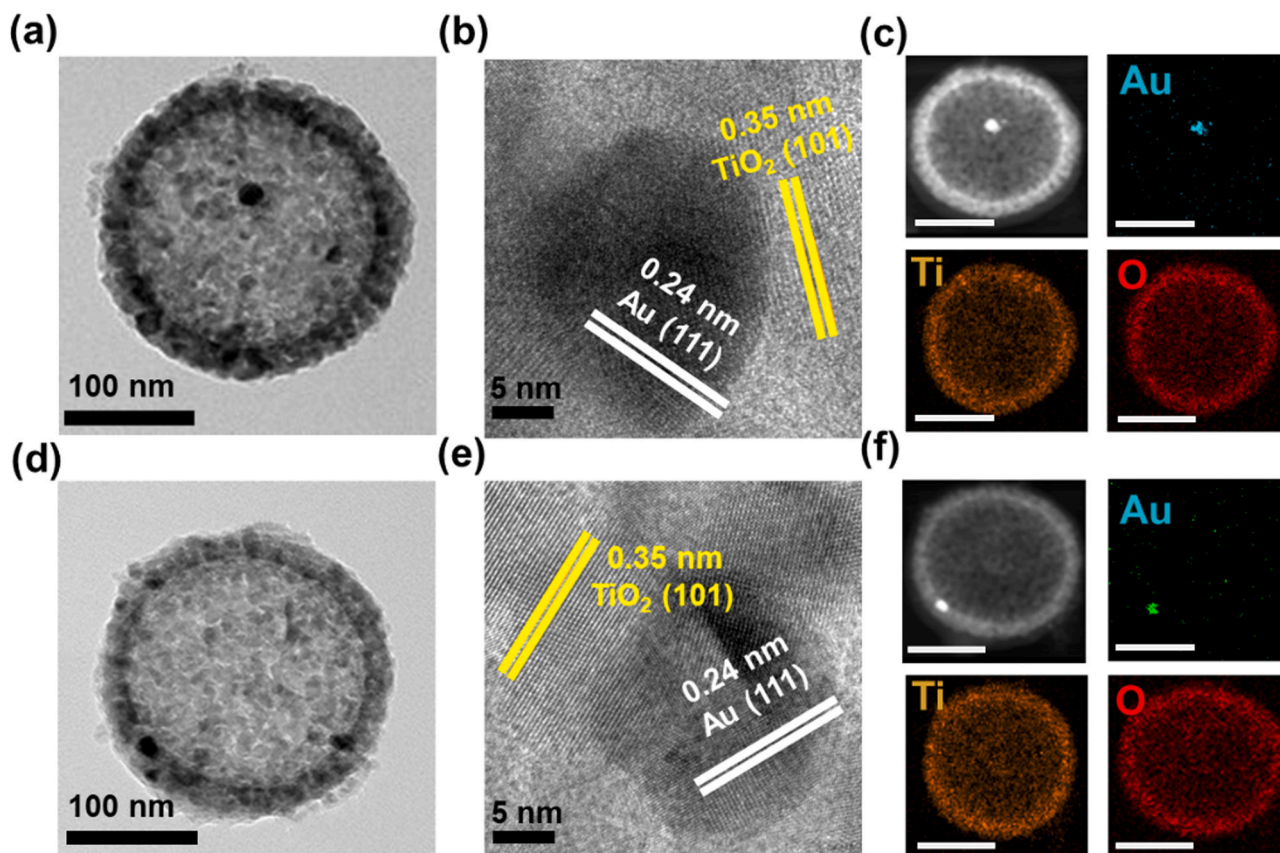


Fig. 2. (a) TEM image, (b) HRTEM image, and (c) HAADF-STEM image and EDS maps of Au, Ti, and O from a single Au@TiO₂ yolk-shell nanohybrid. (d) TEM image, (e) HRTEM image, and (f) HAADF-STEM image and EDS maps of Au, Ti, and O from a single Au@TiO₂ yolk-in-shell nanohybrid. Scale bars in c and f: 100 nm.

yolk-in-shell nanocomposites. The photos and corresponding SEM images of Au@TiO₂ yolk-shell and yolk-in-shell nanohybrids were also given in Fig. S2. Moreover, the TiO₂ shell thicknesses in both structural configurations can be adjusted between 10 and 50 nm (Fig. S3), a critical factor to subsequently evaluate their visible-light photocatalytic performance.

XRD patterns for TiO₂ nanospheres, Au@TiO₂ yolk-shell, and yolk-in-shell nanohybrids are highlighted in Fig. 3a. Seven typical peaks of TiO₂, assigned to (101), (103), (200), (211), (204), (220) and (301) (JCPDS 21-1272), are observed in TiO₂ nanospheres, Au@TiO₂ yolk-shell, and yolk-in-shell nanohybrids, indicating the consistency of composition and phase of the obtained products [41]. The particle size of TiO₂ crystal is further calculated to be 8 nm obtained by Scherrer equation [42], which is consistent with the TEM images (Fig. 2a and d). Moreover, the yolk-shell and yolk-in-shell configurations were further examined using XPS to prove the interaction between gold nanoparticle and TiO₂ shell.

The resulting total electron energy spectra (Fig. S4) reveal that the two types of nanohybrids mainly comprise of Au, Ti, and O elements, in accordance to the results obtained from TEM and EDS analyses. Further comparison of the Au 4f binding energies of pure Au nanoparticles, Au@TiO₂ yolk-shell, and yolk-in-shell nanohybrids (Fig. 3b) reveal that the binding energies of pure Au nanoparticles are 83.7 and 87.4 eV (with the splitting of the 4f doublet of 3.7 eV confirming the metallic state of Au) [43], higher than those of Au@TiO₂ yolk-shell and yolk-in-shell nanohybrids (82.4 and 86.1 eV after correction). Such negative binding energy can attribute to the electron transfer from adjacent TiO₂ surface states to Au clusters via the intimate particle-support interaction because of the large difference in the work function between of Au and TiO₂ [44], suggesting the formation of Schottky heterojunction. Moreover, compared with the TiO₂ nanospheres, the binding energy of O 1s

from Au@TiO₂ yolk-shell or yolk-in-shell nanostructures shown in Fig. S4c, has slight negative shift (about 0.1 eV), due to the interaction between TiO₂ and Au [45]. Thereby, the addition of gold in TiO₂ nanospheres can cooperate with the plasma resonance effect from Au nanoparticles and Schottky heterojunction [46] via the intimate contact between Au and TiO₂, which enable the transfer of hot electrons from Au to TiO₂ and suppressing the recombination of the electron-hole pair [47], thus achieving corresponding synergistic effect for photocatalysis [48].

Besides, it should be noted a small amount of Ti³⁺ and oxygen vacancies existed in Au@TiO₂ yolk-shell and yolk-in-shell nanocomposites were found by XPS and ESR detection, present in Fig. S4b and Fig. S11 respectively. The form of Ti³⁺ and oxygen vacancies may stem from the existence of Au during calcination process [26] and the carbonization of PVP as a stabilizer on the gold surface proved by Fig. S4a, which maybe further take away some oxygen elements in titanium dioxide. As known that such Ti³⁺ and oxygen vacancies act as key active center for photocatalysis discussed in detail later.

Additionally, N₂ adsorption isotherms and related pore size distributions were employed to study their difference in specific surface areas caused by structural differences (Fig. 3c and d, Table S1). The tested results have shown that TiO₂ nanospheres, Au@TiO₂ yolk-shell and yolk-in-shell nanohybrids possess specific surface areas of 107.5 m² g⁻¹, 100.1 m² g⁻¹ and 93.7 m² g⁻¹, respectively, notably with average pore size of 7.6 nm, 14.8 nm and 9.9 nm respectively. In comparison to the TiO₂ counterpart, the two nanohybrids exhibit slightly decreased specific surface areas with notable higher pore diameter. Such higher pore diameter in Au@TiO₂ nanohybrids are due to the additional of Au nanoparticles and are beneficial to facilitate the mass transfer of reactants from the external environment to the encapsulated catalysts. It is worth noting that the distinct difference between these two

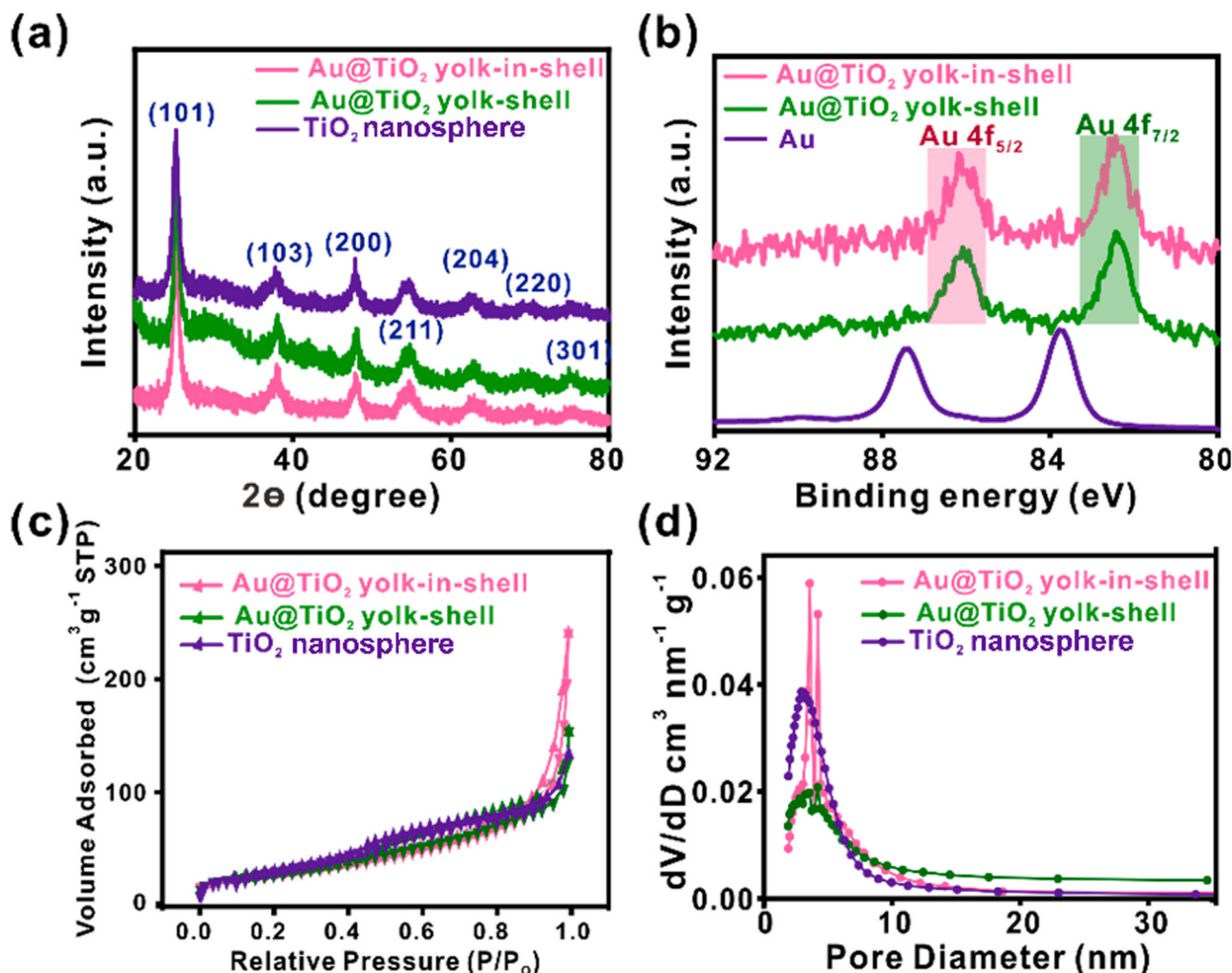


Fig. 3. (a) XRD patterns of TiO₂ nanospheres, Au@TiO₂ yolk-shell (30 nm) and yolk-in-shell (30 nm) nanohybrids. (b) XPS spectra of Au 4f of TiO₂ nanospheres, Au nanoparticles, Au@TiO₂ yolk-shell (30 nm) and yolk-in-shell (30 nm) nanohybrids. (c) N₂ adsorption isotherms and (d) their corresponding pore size distributions of TiO₂ nanospheres, Au@TiO₂ yolk-shell (30 nm) and Au@TiO₂ yolk-in-shell (30 nm) nanohybrids.

nanostructures are the position of single Au nanoparticle in TiO₂ hollow nanosphere. Such structural differences are expected to strongly influence the photocatalytic performance.

We further investigate the optical and electrical properties of nanohybrids which are well-known to be closely related to their photocatalytic properties. Using UV-Vis diffuse reflection spectra (Fig. 4a), the absorption band of Au nanoparticles at 535 nm clearly originated from SPR and can also be observed in Au@TiO₂ yolk-shell and yolk-in-shell nanohybrids. Interestingly, a prominent red shift for the absorption peak of Au (from 535 nm to 595 nm), can be observed in Au@TiO₂ yolk-shell nanohybrids, which is caused by the interaction between Au and TiO₂ shell. It should also be noted that Au@TiO₂ yolk-in-shell nanohybrids have a wider absorption range (about 420–800 nm) than the corresponding Au@TiO₂ yolk-shell nanohybrids, indicating that yolk-in-shell nanostructure enhances the absorption of visible light [49]. The band gap of semiconductors is subsequently calculated according to the Kubelka-Munk method [50]. The indirect band gap energies (Fig. 4b) of Au@TiO₂ yolk-shell, yolk-in-shell nanohybrids and TiO₂ nanospheres are determined at ~ 2.8 eV, 2.8 eV and 3.0 eV, respectively, indicating that the energy band of TiO₂ will be influenced by adding a single Au nanoparticle, although the position of this single Au nanoparticle in TiO₂ rarely contributes to additional energy band change. The different positions of a single Au nanoparticle in nanostructures thus have little effect on the electronic structure, but the unique architectural advantages

are expected to influence the resultant synergetic effect, leading to the divergence of catalytic performance. It should be pointed out that the reduction of TiO₂ band gap after Au loading are attributed to the synergy of the following various factors: (i) a small amount of Ti³⁺ and oxygen vacancies produced by the added Au [51] and the carbonization of PVP (as a stabilizer) on the gold surface respectively, (ii) partial metallization during preparation process [26,52], (iii) the form of the strong built-in electric field due to the connect interaction between Au and TiO₂ [48].

The aforementioned results were further confirmed using photocurrent measurements, which is related to the effectiveness of photoelectron generation in nanocatalysts (Fig. 4c). The Au@TiO₂ yolk-in-shell nanohybrids show about 2 times stronger photocurrent response than the Au@TiO₂ yolk-shell nanohybrids under visible light irradiation, suggesting the yolk-in-shell design with inherent architectural advantages. In contrast, the pure TiO₂ nanospheres have almost no photocurrent response under visible light due to its intrinsically larger band gap. More importantly, time-resolved fluorescence spectra highlight a longer photocarrier lifetime of 8.4 ns in Au@TiO₂ yolk-in-shell nanohybrids [53], which is ~4.6 times longer than the lifetime of photogenerated carriers in Au@TiO₂ yolk-shell nanohybrids (1.8 ns), as shown in Fig. 4d. Thus, the photogenerated electrons tend to transfer to TiO₂ nanoparticles in such yolk-in-shell nanohybrids which is important for efficient photocatalysis. Consequently, the typical Au@TiO₂ yolk-in-shell nanostructure design displays exceedingly excellent optical

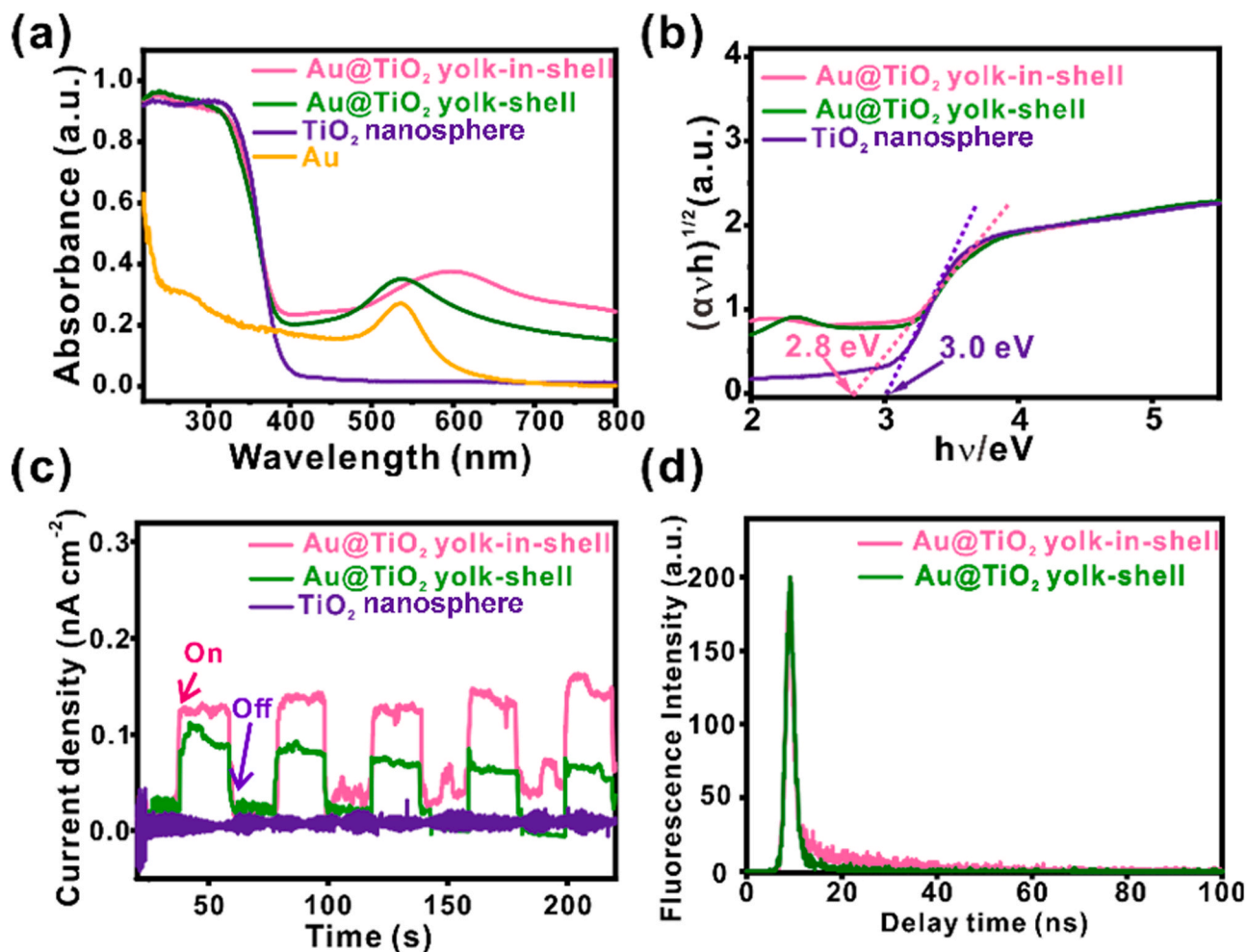


Fig. 4. (a) UV/Vis diffuse reflectance spectra of TiO₂ nanospheres, Au@TiO₂ yolk-shell and yolk-in-shell nanohybrids. (b) Plots of the transformed Kubelka-Munk function versus the energy of light. (c) Transient photocurrents responses of TiO₂ nanospheres, Au@TiO₂ yolk-shell and yolk-in-shell nanohybrids. (d) Fluorescence decays of Au@TiO₂ yolk-shell and yolk-in-shell nanohybrids.

and electrical properties, which are advantageous to visible light photocatalytic performance. In addition, the EIS were used to investigate their electrical properties (Fig. S5). Compared to the other particle

configurations, the Au@TiO₂ yolk-in-shell nanostructure enables minimum charge-transfer resistance favorable for the movement of photo-generated electrons, thanks to the good coordination effect between Au

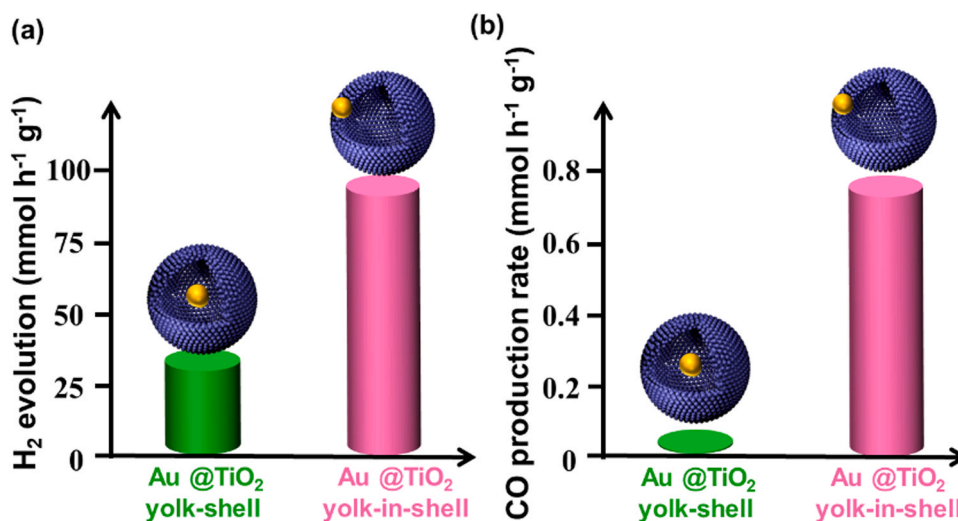


Fig. 5. (a) Photocatalytic hydrogen evolution rates and (b) photocatalytic CO-production activity of Au@TiO₂ yolk-shell and yolk-in-shell nanohybrids under visible light irradiation.

and TiO_2 resulted from the unique structural design. Therefore, the above results have shown that the as-designed Au@TiO_2 yolk-in-shell nanostructures, compared to the yolk-shell nanostructures, display apparent structural advantages critical to realize high-performance catalysis.

3.2. Photocatalytic activity

Finally, H_2O splitting and CO_2 reduction were conducted under visible light to evaluate the photocatalytic performances of TiO_2 nanospheres, Au@TiO_2 yolk-shell and yolk-in-shell nanohybrids (Fig. 5). The rates of product generation (H_2 and CH_4 or CO) have been commonly used to analyze the catalytic performance for H_2O splitting and CO_2

reduction, respectively [15,54,55]. First, the shell thickness of Au@TiO_2 yolk-in-shell nanohybrids has been found to have significant influence on the photocatalytic activity present in Fig. S6c, and the optimized nanostructure of Au@TiO_2 yolk-in-shell (30 nm, Au: 0.04 wt%) nanocatalysts with optimal catalytic performance has been explored in Fig. 5a. It is evidently shown that the as-designed Au@TiO_2 yolk-in-shell nanostructures exhibit an improvement to photocatalytic H_2 evolution activity ($95.6 \text{ mmol h}^{-1} \text{ g}^{-1}$, Au: 0.04 wt%), exceeding that of Au@TiO_2 yolk-shell and TiO_2 nanospheres (Fig. S9) by 3 and 14 times, respectively. To further demonstrate the stability and durability of the Au@TiO_2 yolk-in-shell nanohybrids, four reaction cycles were conducted under the same conditions. The rate of hydrogen production is almost constant in these cycles, highlighting its excellent stability which

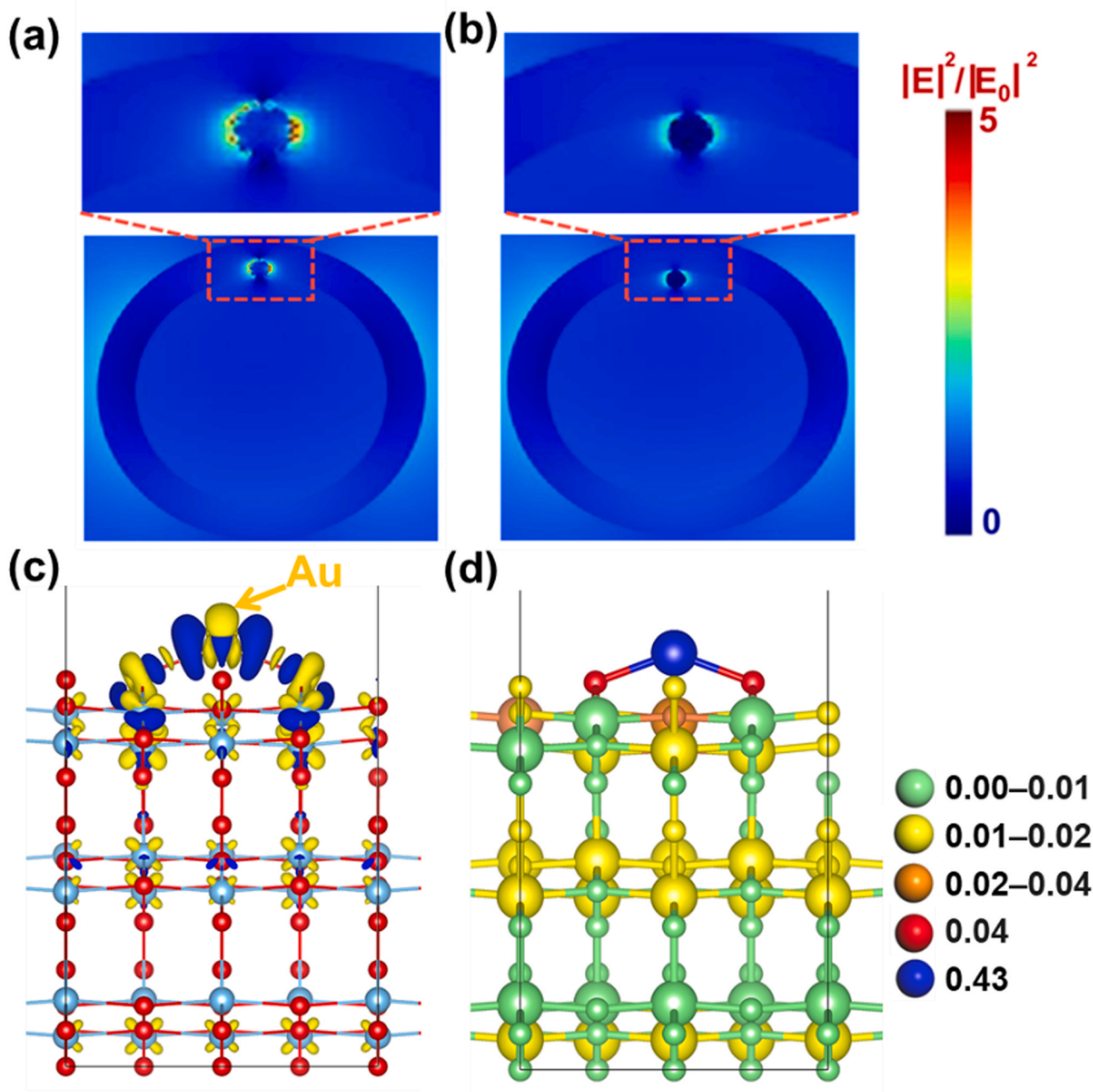


Fig. 6. The distribution of the strongest local enhanced electric field of Au@TiO_2 (a) yolk-in-shell and (b) yolk-shell nanohybrids in the whole simulation region of 420–800 nm. (c) Difference in electron density embedding Au in the anatase TiO_2 (101) surface. Yellow and blue isosurfaces (with an iso-value of 0.005) indicate, respectively, the electron accumulation and depletion regions. (d) Atomic charge distribution in Au@TiO_2 from Bader's topological analysis of the electron density, as indicated by the different colors. (For interpretation of the references to colour in this figure legend, the reader is referred to the web version of this article.)

is also verified by the negligible structural changes in TEM and SEM images after 4 cycles (Fig. S6d and Fig. S7). Moreover, to characterize CO₂ reduction performance of the above materials in Fig. 5b, CH₄ and CO products were monitored and measured. Noticeably, under the visible light irradiation, the CO-production and other potential products are rarely observed in Au@TiO₂ yolk-shell nanohybrids and TiO₂ nanospheres, indicating the lack of ability for CO₂ reduction. Interestingly, the unique Au@TiO₂ yolk-in-shell nanohybrids (Au: 0.04 wt%) exhibit high selectivity (~100%) for CO production (0.75 mmol h⁻¹ g⁻¹) [56–59]. Therefore, the Au@TiO₂ yolk-in-shell nanostructure design is the best catalytic configuration, achieving excellent visible light photocatalytic performance and activating catalytic reaction which is originally inactive.

3.3. FDTD simulations and first-principles calculations

To reveal the mechanism behind for photocatalytic performance improvement in the typical Au@TiO₂ yolk-in-shell nanostructures, FDTD simulations and first-principles calculations have been employed, present in Fig. 6. First, FDTD simulations were utilized to investigate the SPR of Au existing alone in yolk-in-shell and yolk-shell configurations. The corresponding model structure is established, according to TEM images, in Fig. 6a. The simulation results show that the single gold nanoparticle from yolk-in-shell has stronger (around 2 times) electric field compared to the yolk-shell configuration due to lesser extent of shell blocking. It is well-known that SPR commonly depends on the size and morphology of noble metal nanoparticles under the same light field environment. In our case, Au nanoparticles used in both yolk-in-shell and yolk-shell are identical, thus the discrepancy of Au SPR between these two hybrid configurations likely result from the barrier effect of TiO₂ nanospheres on light. Moreover, in order to verify the simulation results of FDTD experimentally, the photothermal experiment on Au@TiO₂ yolk-shell and yolk-in-shell hybrids was further carried out under simulated sunlight for 15 minutes and detected by an IR camera present in Fig. S8. The achieved results indicated that the yolk-in-shell nanostructures display a higher temperature (around 2.7 °C) than the related yolk-shell, indicating the yolk-in-shell nanostructures have stronger photothermal effect thanks to their better plasma resonance, agreeing well with the theoretical results from FDTD simulations. Thus, the prepared Au@TiO₂ yolk-in-shell nanohybrids with better SPR promotes the generation of hot electrons under visible light irradiation for efficient photocatalysis.

Additionally, to insight the additional structural advantage at an atomic level in Au@TiO₂ yolk-in-shell nanohybrids, the first-principles calculations on the change of electronic structures of TiO₂ upon embedding Au were carried out. To keep the model as simple as possible, a single Au atom embedded on the (101) surface of TiO₂ (denoted by Au@TiO₂ for simplicity) was considered, which is then compared with

the corresponding clean surface to reveal the effect of Au on the enhancement of photoactivity of the material. As shown in Fig. 6c and d, a significant amount of electronic charge (0.43 |e⁻|) is transferred from the Au atom to TiO₂, leading to negative charge distribution on TiO₂. This result indicated that an intimate contact will be formed after the Au loading, which is beneficial to electron transfer from Au to TiO₂. Thereby the hot electrons from Au nanoparticle embedded in TiO₂ enable efficiently transferring to the critical conduction band of TiO₂, ultimately promoting the improvement of photocatalytic performance.

3.4. Photocatalytic mechanism

Fig. 7 shows the details of photocatalytic reduction involved in this work for H₂ and CO-production. The effective separation of electron (e⁻) and hole (h⁺), as well as the appropriate and rapid transfer of photo-generated carriers are the key to achieve high efficiency photocatalysis. In our design, excitation of the SPR takes place first under visible-light irradiation, resulting in the generation of the photo-excited electron-hole pairs (e⁻ and h⁺), which are subsequently separated from single Au nanoparticles embedded in TiO₂. Then the induced hot electrons are transferred from the plasmonically excited Au to the adjacent TiO₂ via the formed Schottky heterojunction interface [60]. In this region, it should be noted that the transferred electrons tend to be located on the oxygen vacancies in titanium dioxide, owing to missing oxygen atoms [61]. Finally, the corresponding photocatalytic reduction reaction will take place at the active centers (oxygen vacancies and Ti³⁺). For H₂ production, protons can obtain electrons from the active centers, realizing the generation of H₂. In addition, during CO-production process, the CO₂ molecules adsorbed on TiO₂ are activated by active centers [62], and then meet the electrons with high reduction potential, leading to the spontaneous occurrence of photocatalytic CO production. The enhanced visible light photocatalysis in the Au@TiO₂ yolk-in-shell nanostructure is attributed to three main reasons: (1) promotion of synergy between Au yolk and TiO₂ shell by embedding single Au nanoparticle in TiO₂ shell; (2) enhancement of SPR from Au nanoparticle embedded in TiO₂ shell; (3) efficient hot electron transfer from Au to TiO₂. The unique structural advantages, therefore, offered by yolk-in-shell structure endow promising photocatalysis, especially in the visible light range.

4. Conclusions

In conclusion, a unique yolk-in-shell nanohybrid comprising of single Au nanoparticle as yolk and TiO₂ as shell to boost visible light photocatalysis have been developed. Such Au@TiO₂ yolk-in-shell nanohybrids with precisely-controlled structural features have demonstrated highly efficient visible light photocatalysis, and far surpasses the performances of conventional Au@TiO₂ yolk-shell nanostructures and TiO₂

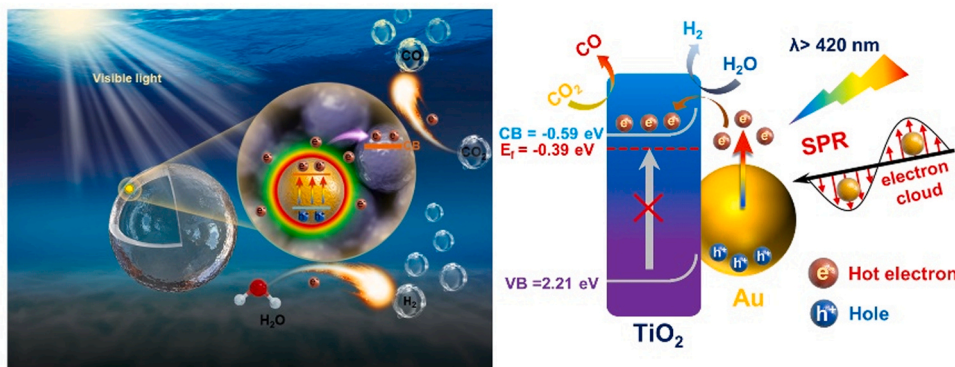


Fig. 7. Schematic diagram of mechanism of visible light photocatalysis induced by the Au@TiO₂ yolk-in-shell nanostructure, involving an energy band structure diagram of such promising photocatalyst.

nanospheres. Results show that the optimal Au@TiO₂ yolk-in-shell nanostructures prefer to promoting the generation of H₂ (95.6 mmol h⁻¹ g⁻¹, Au: 0.04 wt%), beyond other above nanostructures by 3 and 14 times respectively, and realizing selective CO-production (0.75 mmol h⁻¹ g⁻¹). The superior photocatalytic performances result from the unique hierarchical structure of yolk-in-shell design with improved synergistic effect, SPR, and hot electron transfer. This yolk-in-shell design will provide a clear and effective guidance for the construction of next-generation, high-performance nanocatalysts favorable for advanced catalysis.

CRedit authorship contribution statement

Jun Hu: Investigation, Writing – original draft preparation. **Rufang Zhao:** Validation. **Haitao Li:** Supervision, Writing – review & editing. **Zhilong Xu:** Software. **Han Dai:** Validation. **Hua Gao:** Methodology, Validation. **Hongjian Yu:** Investigation. **Ziyao Wang:** Investigation. **Yang Wang:** Methodology, Validation. **Yan Liu:** Data curation. **Jie Han:** Supervision, Resources, Writing – reviewing & editing. **Rong Guo:** Writing – review & editing.

Declaration of Competing Interest

The authors declare that they have no known competing financial interests or personal relationships that could have appeared to influence the work reported in this paper.

Acknowledgements

The authors gratefully acknowledge financial support from the National Natural Science Foundation of China (21922202, 21673202 and 22073080), and the Priority Academic Program Development of Jiangsu Higher Education Institutions. We would also like to acknowledge the technical support received at the Testing Center of Yangzhou University. Y.W. acknowledges the Thousand Talents Plan for Young Professionals of China.

Appendix A. Supporting information

Supplementary data associated with this article can be found in the online version at doi:10.1016/j.apcatb.2021.120869.

References

- [1] A. Li, W. Zhu, C. Li, T. Wang, J. Gong, Rational design of yolk-shell nanostructures for photocatalysis, *Chem. Soc. Rev.* 48 (2019) 1874–1907.
- [2] S. Kim, B.S. Crandall, M.J. Lance, N. Cordonnier, J. Lauterbach, E. Sasmaz, Activity and stability of NiCe@SiO₂ multi-yolk-shell nanotube catalyst for tri-reforming of methane, *Appl. Catal. B: Environ.* 259 (2019), 118037.
- [3] W.N. Wang, C.X. Huang, C.Y. Zhang, M.L. Zhao, J. Zhang, H.J. Chen, Z.B. Zha, T. Zhao, H.S. Qian, Controlled synthesis of upconverting nanoparticles/Zn₃Cd_{1-x}S yolk-shell nanoparticles for efficient photocatalysis driven by NIR light, *Appl. Catal. B: Environ.* 224 (2018) 854–862.
- [4] L.S. Lin, J. Song, H.H. Yang, X. Chen, Yolk-shell nanostructures: design, synthesis, and biomedical applications, *Adv. Mater.* 30 (2018), 1704639.
- [5] M. Waqas, S. Iqbal, A. Bahadur, A. Saeed, M. Raheel, M. Javed, Designing of a spatially separated hetero-junction pseudobrookite (Fe₂TiO₅-TiO₂) yolk-shell hollow spheres as efficient photocatalyst for water oxidation reaction, *Appl. Catal. B: Environ.* 219 (2017) 30–35.
- [6] K. Cui, W. Zhong, L. Li, Z. Zhuang, L. Li, J. Bi, Y. Yu, Well-defined metal nanoparticles@covalent organic framework yolk-shell nanocages by ZIF-8 template as catalytic nanoreactors, *Small* 15 (2019), 1804419.
- [7] W. Wang, B. Xu, X. Pan, J. Zhang, H. Liu, Solvent-dependent adsorption-driven mechanism for MOFs-based yolk-shell nanostructures, *Angew. Chem. Int. Ed.* 60 (2021) 7802–7808.
- [8] D. Du, W. Shi, L. Wang, J. Zhang, Yolk-shell structured Fe₃O₄@void@TiO₂ as a photo-Fenton-like catalyst for the extremely efficient elimination of tetracycline, *Appl. Catal. B: Environ.* 200 (2017) 484–492.
- [9] Q.C. Do, D.G. Kim, S.O. Ko, Nonsacrificial template synthesis of magnetic-based yolk-shell nanostructures for the removal of acetaminophen in Fenton-like systems, *ACS Appl. Mater. Interfaces* 9 (2017) 28508–28518.
- [10] N. Tian, K. Xiao, Y. Zhang, X. Lu, L. Ye, P. Gao, T. Ma, H. Huang, Reactive sites rich porous tubular yolk-shell g-C₃N₄ via precursor recrystallization mediated microstructure engineering for photoreduction, *Appl. Catal. B: Environ.* 253 (2019) 196–205.
- [11] C. Wang, X. Jie, Y. Qiu, Y. Zhao, H.A. Al-Megren, S. Alshihri, P.P. Edwards, T. Xiao, The importance of inner cavity space within Ni@SiO₂ nanocapsule catalysts for excellent coking resistance in the high-space-velocity dry reforming of methane, *Appl. Catal. B: Environ.* 259 (2019), 118019.
- [12] A. Li, T. Wang, X. Chang, W. Cai, P. Zhang, J. Zhang, J. Gong, Spatial separation of oxidation and reduction co-catalysts for efficient charge separation: Pt@TiO₂@MnOx hollow spheres for photocatalytic reactions, *Chem. Sci.* 7 (2016) 890–895.
- [13] A. Ziarati, A. Badiei, R. Luque, Engineered bi-functional hydrophilic/hydrophobic yolk@shell architectures: a rational strategy for non-time dependent ultra selective photocatalytic oxidation, *Appl. Catal. B: Environ.* 240 (2019) 72–78.
- [14] Y.-H. Chiu, S.B. Naghadeh, S.A. Lindley, T.-H. Lai, M.-Y. Kuo, K.-D. Chang, J. Z. Zhang, Y.-J. Hsu, Yolk-shell nanostructures as an emerging photocatalyst paradigm for solar hydrogen generation, *Nano Energy* 62 (2019) 289–298.
- [15] X. Cai, Z. Zeng, Y. Liu, Z. Li, X. Gu, Y. Zhao, L. Mao, J. Zhang, Visible-light-driven water splitting by yolk-shelled ZnIn₂S₄-based heterostructure without noble-metal co-catalyst and sacrificial agent, *Appl. Catal. B: Environ.* 297 (2021), 120391.
- [16] L.S. Lin, X. Yang, Z. Zhou, Z. Yang, O. Jacobson, Y. Liu, A. Yang, G. Niu, J. Song, H. H. Yang, X. Chen, Yolk-shell nanostructure: an ideal architecture to achieve harmonious integration of magnetic-plasmonic hybrid theranostic platform, *Adv. Mater.* 29 (2017), 1606681.
- [17] G. Wan, X. Peng, M. Zeng, L. Yu, K. Wang, X. Li, G. Wang, The preparation of Au@TiO₂ yolk-shell nanostructure and its applications for degradation and detection of methylene blue, *Nanoscale* 12 (2017) 535.
- [18] G. Li, Z. Tang, Noble metal nanoparticle@metal oxide core/yolk-shell nanostructures as catalysts: recent progress and perspective, *Nanoscale* 6 (2014) 3995–4011.
- [19] S. Li, J. Niu, Y.C. Zhao, K.P. So, C. Wang, C.A. Wang, J. Li, High-rate aluminium yolk-shell nanoparticle anode for Li-ion battery with long cycle life and ultrahigh capacity, *Nat. Commun.* 6 (2015) 7872.
- [20] J. Li, S. Song, Y. Long, L. Wu, X. Wang, Y. Xing, R. Jin, X. Liu, H. Zhang, Investigating the hybrid-structure-effect of CeO₂-encapsulated Au nanostructures on the transfer coupling of nitrobenzene, *Adv. Mater.* 30 (2018), 1704416.
- [21] Z. Chen, J. Wang, G. Zhai, W. An, Y. Men, Hierarchical yolk-shell WO₃ microspheres with highly enhanced photoactivity for selective alcohol oxidations, *Appl. Catal. B: Environ.* 218 (2017) 825–832.
- [22] X. Feng, M. Tian, C. He, L. Li, J.-W. Shi, Y. Yu, J. Cheng, Yolk-shell-like mesoporous CoCrO_x with superior activity and chlorine resistance in dichloromethane destruction, *Appl. Catal. B: Environ.* 264 (2020), 118493.
- [23] J. Sun, J. Hu, J. Han, G. Yuan, R. Guo, Dumbbell-like Pt-Fe₃O₄ nanoparticles encapsulated in N-doped carbon hollow nanospheres as a novel yolk@shell nanostructure toward high-performance nanocatalysis, *Langmuir* 35 (2019) 12704–12710.
- [24] X. Sun, J. Han, R. Guo, A mini review on yolk-shell structured nanocatalysts, *Front. Chem.* 8 (2020), 606044.
- [25] Z. Zhang, Y. Du, Q.C. Wang, J. Xu, Y.N. Zhou, J. Bao, J. Shen, X. Zhou, A yolk-shell-structured FePO₄ cathode for high-rate and long-cycling sodium-ion batteries, *Angew. Chem. Int. Ed.* 59 (2020) 17504–17510.
- [26] Y. Wang, C. Yang, A. Chen, W. Pu, J. Gong, Influence of yolk-shell Au@TiO₂ structure induced photocatalytic activity towards gaseous pollutant degradation under visible light, *Appl. Catal. B: Environ.* 251 (2019) 57–65.
- [27] J. Han, M. Wang, R. Chen, N. Han, R. Guo, Beyond yolk-shell nanostructure: a single Au nanoparticle encapsulated in the porous shell of polymer hollow spheres with remarkably improved catalytic efficiency and recyclability, *Chem. Commun.* 50 (2014) 8295–8298.
- [28] J. Hu, R. Li, J. Han, J. Sun, Y. Wang, L. Yu, R. Guo, Yolk-shell or yolk-in-shell nanocatalysts? A proof-of-concept study, *J. Mater. Chem. A* 8 (2020) 10217–10225.
- [29] Q. Yue, J. Li, Y. Zhang, X. Cheng, X. Chen, P. Pan, J. Su, A.A. Elzatahry, A. Alghamdi, Y. Deng, D. Zhao, Plasmonics-inspired nanoengineering of functional yolk-shell microspheres with magnetic core and mesoporous silica shell, *J. Am. Chem. Soc.* 139 (2017) 15486–15493.
- [30] C. Jin, J. Han, F. Chu, X. Wang, R. Guo, Fe₃O₄@PANI hybrid shell as a multifunctional support for Au nanocatalysts with a remarkably improved catalytic performance, *Langmuir* 33 (2017) 4520–4527.
- [31] Y. Liu, J. Han, L. Fan, Y. Li, R. Guo, Pomegranate-like multicore-shell Mn₃O₄ encapsulated mesoporous N-doped carbon nanospheres with an internal void space for high-performance lithium-ion batteries, *Chem. Commun.* 55 (2019) 8064–8067.
- [32] G. Wang, Y. Sun, D. Li, H.W. Liang, R. Dong, X. Feng, K. Mullen, Controlled synthesis of N-doped carbon nanospheres with tailored mesopores through self-assembly of colloidal silica, *Angew. Chem. Int. Ed.* 54 (2015) 15191–15196.
- [33] M. Yang, J. Ma, Z. Niu, X. Dong, H. Xu, Z. Meng, Z. Jin, Y. Lu, Z. Hu, Z. Yang, Synthesis of spheres with complex structures using hollow latex cages as templates, *Adv. Funct. Mater.* 15 (2005) 1523–1528.
- [34] G. Kresse, J. Furthmüller, Efficient iterative schemes for ab initio total-energy calculations using a plane-wave basis set, *Phys. Rev. B* 54 (1996) 11169–11186.
- [35] G. Kresse, J. Furthmüller, Efficiency of ab-initio total energy calculations for metals and semiconductors using a plane-wave basis set, *Comput. Mater. Sci.* 6 (1996) 15–50.
- [36] P.E. Blöchl, Projector augmented-wave method, *Phys. Rev. B* 50 (1994) 17953–17979.

- [37] G. Kresse, D. Joubert, From ultrasoft pseudopotentials to the projector augmented-wave method, *Phys. Rev. B* 59 (1999) 1758–1775.
- [38] J.P. Perdew, K. Burke, M. Ernzerhof, Generalized gradient approximation made simple, *Phys. Rev. Lett.* 77 (1996) 3865–3868.
- [39] J. Heyd, G.E. Scuseria, M. Ernzerhof, Hybrid functionals based on a screened Coulomb potential, *J. Chem. Phys.* 118 (2003) 8207–8215.
- [40] H.J. Monkhorst, J.D. Pack, Special points for Brillouin-zone integrations, *Phys. Rev. B* 13 (1976) 5188–5192.
- [41] Q. Zhao, Q. Zhang, C. Du, S. Sun, J.D. Steinkruger, C. Zhou, S. Yang, Synergistic effect of dual particle-size AuNPs on TiO₂ for efficient photocatalytic hydrogen evolution, *Nanomaterials* 9 (2019) 499.
- [42] S.R. Dhage, R. Pasricha, V. Ravi, Synthesis of ultrafine TiO₂ by citrate gel method, *Mater. Res. Bull.* 38 (2003) 1623–1628.
- [43] P. She, J. Qin, H. Rao, B. Guan, J. Yu, Spatially separated bimetallic cocatalysts on hollow-structured TiO₂ for photocatalytic hydrogen generation, *Mater. Chem. Front.* 4 (2020) 1671–1678.
- [44] B. Tian, J. Zhang, T. Tong, F. Chen, Preparation of Au/TiO₂ catalysts from Au(I)-thiosulfate complex and study of their photocatalytic activity for the degradation of methyl orange, *Appl. Catal. B: Environ.* 79 (2008) 394–401.
- [45] G. Yang, H. Ding, D. Chen, J. Feng, Q. Hao, Y. Zhu, Construction of urchin-like ZnIn₂S₄-Au-TiO₂ heterostructure with enhanced activity for photocatalytic hydrogen evolution, *Appl. Catal. B: Environ.* 234 (2018) 260–267.
- [46] J.D. Xiao, L. Han, J. Luo, S.H. Yu, H.L. Jiang, Integration of plasmonic effects and Schottky junctions into metal-organic framework composites: steering charge flow for enhanced visible-light photocatalysis, *Angew. Chem. Int. Ed.* 57 (2018) 1103–1107.
- [47] M. Wang, J. Han, H. Xiong, R. Guo, Yolk@shell nanoarchitecture of Au@r-GO/TiO₂ hybrids as powerful visible light photocatalysts, *Langmuir* 31 (2015) 6220–6222.
- [48] A. Meng, L. Zhang, B. Cheng, J. Yu, Dual cocatalysts in TiO₂ photocatalysis, *Adv. Mater.* 31 (2019), 1807660.
- [49] X. Cai, Q. Chen, R. Wang, A. Wang, J. Wang, S. Zhong, Y. Liu, J. Chen, S. Bai, Integration of plasmonic metal and cocatalyst: An efficient strategy for boosting the visible and broad-spectrum photocatalytic H₂ evolution, *Adv. Mater. Interfaces* 6 (2019), 1900775.
- [50] M. Wang, Z. Cui, M. Yang, L. Lin, X. Chen, M. Wang, J. Han, Core/shell structured CdS/polydopamine/TiO₂ ternary hybrids as highly active visible-light photocatalysis, *J. Colloid Interface Sci.* 544 (2019) 1–7.
- [51] X. Li, J. Yu, M. Jaroniec, X. Chen, Cocatalysts for selective photoreduction of CO₂ into solar fuels, *Chem. Rev.* 119 (2019) 3962–4179.
- [52] R.S. Sonawane, M.K. Dongare, Sol-gel synthesis of Au/TiO₂ thin films for photocatalytic degradation of phenol in sunlight, *J. Mol. Catal. A-Chem.* 243 (2006) 68–76.
- [53] C. Yang, Y. Meng, S. Xia, G. Pan, Hot carrier transfer-induced photodegradation at a thiolated Au/TiO₂ interface under X-ray irradiation, *J. Phys. Chem. B* 124 (2020) 22212–22220.
- [54] M. Liang, T. Borjigin, Y. Zhang, H. Liu, B. Liu, H. Guo, Z-Scheme Au@void@g-C₃N₄/SnS yolk-shell heterostructures for superior photocatalytic CO₂ reduction under visible light, *ACS Appl. Mater. Interfaces* 10 (2018) 34123–34131.
- [55] A. Wang, S. Wu, J. Dong, R. Wang, J. Wang, J. Zhang, S. Zhong, S. Bai, Interfacial facet engineering on the Schottky barrier between plasmonic Au and TiO₂ in boosting the photocatalytic CO₂ reduction under ultraviolet and visible light irradiation, *Chem. Eng. J.* 404 (2021), 127145.
- [56] X. Chang, T. Wang, P. Yang, G. Zhang, J. Gong, The development of cocatalysts for photoelectrochemical CO₂ reduction, *Adv. Mater.* 31 (2019), 1804710.
- [57] F. Li, H. Zhou, J. Fan, Q. Xiang, Amine-functionalized graphitic carbon nitride decorated with small-sized Au nanoparticles for photocatalytic CO₂ reduction, *J. Colloid Interface Sci.* 570 (2020) 11–19.
- [58] J. Ran, M. Jaroniec, S. Qiao, Cocatalysts in semiconductor-based photocatalytic CO₂ reduction: achievements, challenges, and opportunities, *Adv. Mater.* 30 (2018), 1704649.
- [59] Y. Li, B. Li, D. Zhang, L. Cheng, Q. Xiang, Crystalline carbon nitride supported copper single atoms for photocatalytic CO₂ reduction with nearly 100% CO selectivity, *ACS Nano* 14 (2020) 10552–10561.
- [60] W. Hou, W.H. Hung, P. Pavaskar, A. Goepfert, M. Aykol, S.B. Cronin, Photocatalytic conversion of CO₂ to hydrocarbon fuels via plasmon-enhanced absorption and metallic interband transitions, *ACS Catal.* 1 (2011) 929–936.
- [61] D. Zhang, X. Ma, H. Zhang, Y. Liao, Q. Xiang, Enhanced photocatalytic hydrogen evolution activity of carbon and nitrogen self-doped TiO₂ hollow sphere with the creation of oxygen vacancy and Ti³⁺, *Mater. Today Energy* 10 (2018) 132–140.
- [62] N.N. Vu, S. Kaliaguine, T.O. Do, Critical aspects and recent advances in structural engineering of photocatalysts for sunlight-driven photocatalytic reduction of CO₂ into fuels, *Adv. Funct. Mater.* 29 (2019), 1901825.